THE JOURNAL OF PHYSICAL CHEMISTRY A

Article

pubs.acs.org/JPCA

Solvation and Spectral Line Shifts of Chromium Atoms in Helium Droplets Based on a Density Functional Theory Approach

Martin Ratschek,*[,†] Johann V. Pototschnig,[†] Andreas W. Hauser,[‡] and Wolfgang E. Ernst*[,†]

[†]Institute of Experimental Physics, Graz University of Technology, Petersgasse 16, A−8010 Graz, Austria

[‡]Department of Chemical and Biomolecular Engineering, University of California, 45 Gilman Hall, Berkeley, California 94720-1462, United States

ABSTRACT: The interaction of an electronically excited, single chromium (Cr) atom with superfluid helium nanodroplets of various size (10 to 2000 helium (He) atoms) is studied with helium density functional theory. Solvation energies and pseudo-diatomic potential energy surfaces are determined for Cr in its ground state as well as in the y^7P, a^5S, and y^5P excited states. The necessary Cr−He pair potentials are calculated by standard methods of molecular orbital-based electronic structure theory. In its electronic ground state the Cr atom is found to be fully submerged in the droplet. A solvation shell structure is derived from fluctuations in the radial helium density. Electronic excitations of an embedded Cr atom are simulated by confronting the relaxed helium density (ρ_{He}), obtained for Cr in the ground state, with interaction pair potentials of excited states. The resulting energy shifts for the transitions $z^7P \leftarrow a^7S$, $y^7P \leftarrow a^7S$, $z^5P \leftarrow a^5S$, and $y^5P \leftarrow a^5S$ are compared to recent fluorescence and photoionization experiments.

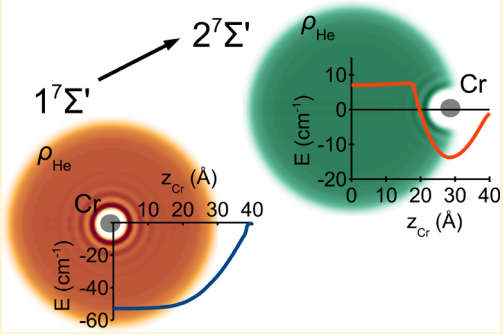

1. INTRODUCTION

Chromium, a very versatile transition metal due to its half filled 3d and 4s shells, is found in 9 different oxidation states, ranging from −2 to 6. Its ground state is of septet multiplicity (a^7S, [Ar]$3d^54s$), with an outstanding magnetic moment of 6 μ_B. While Cr clusters are mostly formed in antiferromagnetic states,[1,2] the principal possibility to create high-spin nanoparticles[3] makes them a technologically interesting target. In this context, the experimental methods of helium nanodroplet isolation spectroscopy[4] offer a 2-fold advantage for studying cluster formation and manipulation. First, it has been shown that cluster formation on helium nanodroplets (He_N) is spin selective, with a clear preference for weakly bound high spin states.[3,5−8] Second, single species of the formed clusters are made spectroscopically accessible at very low temperature due to the cold He environment.[4,9] Recent experimental investigations of Cr on He_N in our group were based on mass spectroscopy,[10] followed by photoionization and fluorescence studies.[11−13] The particularly complex interaction between Cr and the He environment, with Cr turning out to be a borderline species in terms of its actual position on the droplet, triggered this theoretical study.

We investigate the influence of the He_N environment on Cr in its ground state and selected electronically excited states of the septet and quintet spin manifold by means of helium density functional theory (DFT). A powerful alternative to this approach are quantum Monte Carlo methods,[14] as has recently been shown for the $^3\Sigma_u$ high spin state of Rb_2.[15,16] However, though more qualitative in its analysis, the DFT approach provides us with a simple model of electronic excitation that allows us to interpret and understand basic spectroscopic features of the Cr−He_N system. Similar studies (ground states only) have been published recently for the Rb−He_N and Xe−Rb−He_N system.[17,18]

2. COMPUTATIONAL METHODS

Helium density functional theory is applied to calculate free energies and density profiles for Cr-doped helium nanodroplets consisting of up to 2000 He atoms. Note that, in contrast to the common DFT methods of electronic structure theory, the energy is not written as a functional of the electronic but of the atomic density.[19] Two functionals found application in the helium droplet community. The Orsay−Paris functional was proposed in refs 20−23 for both He isotopes. Our choice, the Orsay−Trento functional, was specifically tailored for isotopically homogeneous ^{4}He systems, improving the description of static and dynamic properties of liquid ^{4}He.[24]

In our computational approach the free energy of a doped He droplet is minimized for a given dopant position. The free energy $F[\rho]$, a functional of the helium density ρ, may be written as

$$F[\rho] = E[\rho] + U_{ext}[\rho] - \mu N[\rho] - \vec{F}\cdot\vec{R}[\rho] \quad (1)$$

Special Issue: Franco Gianturco Festschrift

Received: April 7, 2014
Revised: June 6, 2014
Published: June 6, 2014

   dx.doi.org/10.1021/jp5034036 | J. Phys. Chem. A 2014, 118, 6622−6631

with $E[\rho]$ as the Orsay−Trento density functional and $U_{ext}[\rho]$ as an external potential, which describes the interaction between the droplet and the dopant. Two constraints, the conservation of the particle number (N) and the center of mass ($\vec{R}$), appear as terms on the right-hand side, together with their corresponding Lagrange parameters, the chemical potential μ and the retaining force $\vec{F}$, respectively. The retaining force $\vec{F}$ fixes the distance between the center of mass of the He_N and the dopant to a predetermined value enabling the calculation of the Cr−He_N potential energy surface (PES). The DFT code we use was developed by Dalfovo and expanded by Lehmann and Schmied.[25,26] More recent developments in the field are a fully variational DFT,[27] which provides an improved description of strongly interacting dopants and the liquid−solid transition, and a time-dependent DFT code, which allows dynamical treatments of He systems.[28]

2.1. Ab Initio Calculations for the Cr−He Diatomic Molecule. Any interaction between the chromium atom in a certain electronic state and the helium droplet is represented by $U_{ext}[\rho]$ in eq 1. This term contains a density-weighted summation over Cr−He pair energy contributions. The latter can be obtained from diatomic Cr−He potential energy curves, with Cr in the relevant electronic state. The wanted Cr−He potential curves for the $X^7\Sigma^+$ ground state (a^7S) and the lowest state in the quintet spin manifold, $1^5\Sigma^+$ (a^5S), were taken from ref 29. Both are corrected for relativistic effects and finiteness of the basis set. The remaining excited states, $2^7\Sigma^+/1^7\Pi$, $4^7\Sigma^+/4^7\Pi$, $5^5\Sigma^+/5^5\Pi$, and $6^5\Sigma^+/6^5\Pi$, which correspond to the atomic excitations z^7P, y^7P, z^5P, and y^5P, were calculated with the Molpro quantum chemistry package[30] according to the following procedure: A state-averaged complete active space multiconfigurational selfconsistent field calculation (CASSCF)[33,34] was performed with the aug-cc-pVTZ-DK[31,32] basis set, followed by second order multireference configuration interaction calculation (MRCI).[33] (The Π-states in the septet-multiplicity were unsuccessfully treated with coupled cluster (CC) methods. The open shell character of Cr prohibits a reliable treatment with CC methods as shown in ref 29.)

2.2. DIM Approach. The interaction between He_N and the dopant appears as $U_{ext}[\rho]$ in eq 1. In our approach, this external potential is approximated via a density-weighted integration of Cr−He pair potential energies over space:

$$U_{ext}[\rho] = \int V_{pair}(\vec{r})\rho(\vec{r})\mathrm{d}\vec{r} \tag{2}$$

We set the origin of our coordinate system to the dopant position. For a He_N-centered atom in an electronic S state the choice of spherical coordinates is convenient since the integrand does not have any angular dependence, which reduces the problem to an integration over the radial component only. However, a slight displacement of the dopant from the droplet center immediately results in a breakdown of spherical symmetry, and the problem is best treated in cylindrical coordinates. Note that in this case the pair potential V_{pair} is still spherically symmetric (but the density $\rho(\vec{r})$ is not) and that a single coordinate is sufficient to describe the interaction. This situation changes if we allow the dopant atom to be in electronically excited states with angular momenta larger than zero. Now, the pair potential itself varies in two coordinates and needs to be integrated in two dimensions. For convenience, we choose a definition according to the illustration in Figure 1, with r as the distance between the Cr atom and a source point of He density, and Θ as the angle between vector $\vec{r}$ and the internuclear axis in a pseudo-diatomic picture.[35] This axis is defined as the vector between the dopant position and the center of mass calculated for a given helium density distribution.

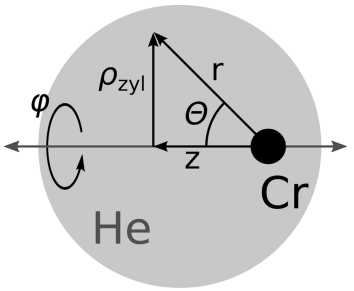

Figure 1. Coordinates for the integration over the He−Cr pair potential for electronic states with angular momenta larger than zero.

Finally, the actual two-dimensional interaction potential V_{pair} needs to be derived for each value of Λ, the projection of the angular momentum onto the internuclear axis. Here we follow the diatomics in molecules (DIM) approach first proposed by Ellison in refs 36 and 37, by now a well-established method within the helium droplet community.[28,38−42] In our concrete case of atomic P excitations, the necessary Cr−He Σ and Π states are represented by ab initio PESs $V_\Sigma(r)$ and $V_\Pi(r)$ obtained from the Molpro quantum chemistry package. They can be combined to form on-droplet Σ′ and Π′ states, expressed by two two-dimensional PESs $V_{\Sigma'}(r, \Theta)$ and $V_{\Pi'}(r, \Theta)$:

$$V_{\Sigma'}(r, \Theta) = V_\Sigma(r)\cos^2\Theta + V_\Pi(r)\sin^2\Theta$$
$$V_{\Pi'}(r, \Theta) = V_\Pi(r)\cos^2\Theta + \frac{1}{2}[V_\Sigma(r) + V_\Pi(r)]\sin^2\Theta \tag{3}$$

A constant factor stemming from the formal integration over the azimuth φ has already been adsorbed in these equations. According to eq 2, these PESs need to be integrated over spatial coordinates for the final evaluation of $U_{ext}[\rho]$. This is most easily done in cylindrical coordinates, with the interatomic axis as the z axis in the new coordinate system. Note that the coordinate transformations

$$r = \sqrt{z^2 + \rho_{zyl}^2}$$
$$\Theta = \arctan(\rho_{zyl}/z), \tag{4}$$

give rise to a pole in the integrand for arbitrary He densities. However, since the He density is zero at the dopant position by necessity, this point can be excluded.

2.3. Frozen Droplet: An Approximation to Atomic Excitations. A series of DFT calculations, performed as described above, but repeated for different interatomic distances between droplet and Cr atom, allows us to determine the preferred localization of the dopant for a given interaction potential. An effective Cr−He_N PES is obtained, from which we derive the solvation energy as the difference between free energies of the doped and the undoped droplet. We refer to this type of calculation as relaxed since the He density is fully adapted to effects introduced by U_{ext}, the interaction potential of the dopant.

In contrast to these relaxation calculations, "frozen" droplet calculations are single-point energy evaluations without

dx.doi.org/10.1021/jp5034036 | J. Phys. Chem. A 2014, 118, 6622−6631

readjustment of the He density, although the interaction potential might have changed. Such an evaluation can be interpreted as a zeroth-order approach to the electronic excitation of a Cr atom on He_N: The optical excitation of the dopant is fast compared to the relaxation of the droplet.[28,43] Therefore, the He_N density distribution can be assumed to be constant during excitation. To calculate the shifts in the transition energy for a certain electronic excitation from atomic state A to B, we let the doped He_N relax in state A at first. The obtained density is then used to evaluate the energies for states B and A, and their energetic difference is interpreted as on-droplet excitation energy.

Line broadening effects have been extensively studied in refs 39 and 40. Two contributions can be identified: The thermal motion of the dopant within the He_N matrix results in a minor line broadening, but oscillations of the He_N bubble around the dopant lead to additional shifts and line-broadening especially for submerged dopants. A larger line-broadening effect is caused by the spherically symmetric breathing mode.[40] We limit our investigation to the droplet-centered atomic S state a^7S and spherical symmetry in the initial state and follow a simplified approach of ref 40. We start with the ground state equilibrium density distribution of the doped He_N $\rho(r)$. The breathing mode bubble oscillation is implemented by applying a displacement α on the density distribution including a renormalization:

$$\rho'(r, \alpha) = \rho(r + \alpha)\mathcal{N}^{-1}$$

$$\mathcal{N} = N^{-1}4\pi \int (r + \alpha)^2 \rho'(r, \alpha)\mathrm{d}r$$

Both the energy of the ground state $U_{ext,GS}[\rho'(r, \alpha)]$ and the excited state $U_{ext,ES}[\rho'(r, \alpha)]$ were calculated within the frozen droplet approach according to eq 2. The transition energies for specific bubble deformations (α) are then obtained by

$$E_m(\alpha) = U_{ext,ES}[\rho'(r, \alpha)] - U_{ext,GS}[\rho'(r, \alpha)] + E_{m,A} \quad (5)$$

with $E_{m,A}$ being the energy of the atomic transition with the identifier m, which is not taken into account in eq 2. In order to calculate the probability for displacements α, the bubble oscillation is described by a harmonic oscillator with the wave function ψ_0 (r), the hydrodynamic mass M_0^*, the angular frequency ω_0, and the equilibrium bubble radius R_0. For the calculation of the broadening the potentials are assumed to be of Lennard-Jones type $(r_{min}, \epsilon_{min})$ resulting in the following equations:

$$R_0 = 2^{-1/6} r_{min} \quad (6)$$

$$B = 4\pi\rho_{He,b} m_{He} {R_0}^5 \quad (7)$$

$$C = 8\pi\sigma_{He} {R_0}^2 (1 + 12\lambda_A) \quad (8)$$

The density[19,44] $\rho_{He,b} = 0.0218$ Å^{-3} and surface tension[45] $\sigma_{He} = 0.179$ cm^{-1} Å^{-2} of bulk liquid He are used. The Ancilotto parameter λ_A is discussed in section 2.4, and its value can be found in Table 1. With these quantities, the energy $\hbar\omega_0$ and the hydrodynamic mass M_0^* of the breathing mode can be determined:

$$\omega_0 = 2\sqrt{C/B} \quad (9)$$

$$M_0^* = B/{R_0}^2 \quad (10)$$

Table 1. Ancilotto (λ_A) and de Boer (λ_B) Parameters Obtained for Selected States of Diatomic Cr−He

lim.	term	r_{min}	ε_d	λ_B	λ_A
a ^7S	X $^7\Sigma^+$ [a]	5.038	4.88	0.21	2.69
	X $^7\Sigma^+$	5.145	4.72	0.23	2.41
z $^7P^\circ$	2 $^7\Sigma^+$	7.781	1.02	0.42	0.87
	1 $^7\Pi$	1.983	672.67	0.01	146.20
y $^7P^\circ$	4 $^7\Sigma^+$	7.575	1.34	0.34	1.11
	4 $^7\Pi$	6.399	2.50	0.25	1.75
a ^5S	1 $^5\Sigma^+$	6.067	1,48	0.47	0.98
z $^5P^\circ$	5 $^5\Sigma^+$	8.067	0.86	0.46	0.76
	5 $^5\Pi$	3.041	79.67	0.04	26.56
y $^5P^\circ$	6 $^5\Sigma^+$	6.668	1.99	0.29	1.46
	6 $^5\Pi$	6.408	2.28	0.28	1.60

[a]Calculated at the CCSD(T) level. All others are based on MRCI results.

The following wave function can then be applied for the breathing deformation:

$$|\psi(\alpha)|^2 = \left(\frac{M_0^*\omega_0}{\pi\hbar}\right)^{1/2} \exp\left(\frac{M_0^*\omega_0}{\hbar}\alpha^2\right) \quad (11)$$

A combination of eq 5 and 11 allows to calculate the spectrum:

$$I(\omega) = \sum_m \int |\psi(\alpha)|^2 \delta(\omega - E_m(\alpha))\mathrm{d}\alpha \quad (12)$$

2.4. Comparison to Basic Descriptors. Two basic descriptors, the Ancilotto parameter λ_A and the de Boer factor λ_B, are sometimes applied to obtain first predictions for the interaction of a certain dopant with He_N.[46] The only input needed for this estimation are basic parameters of the corresponding He−dopant diatomic PES. λ_A is a dimensionless parameter, formed by the ratio of the free energy gain due to the dopant−matrix interaction and the free energy cost due to the formation of a bubble around the dopant. The dopant−matrix interaction is based on a diatomic PES with spherical symmetry. Therefore, λ_A relates the PES properties, the well depth ε_d and the equilibrium separation r_{min}, the number density of the matrix particles ρ_{num}, and the surface tension σ as follows:

$$\lambda_A = \frac{\rho_{num}\varepsilon_d r_{min}}{\sigma 2^{1/6}} \quad (13)$$

For liquid ^{4}He a threshold value of $\lambda_A = 1.9$ has been found, distinguishing between surface residing $(\lambda_A < 1.9)$ and submerging $(\lambda_A > 1.9)$ species. Simplifications of λ_A are the assumption of spherically symmetric and idealized Lennard−Jones-type interaction and the neglect of quantum effects such as zero point energy. The latter can be estimated via the de Boer parameter[46] (λ_B), which relates ε_d, r_{min}, the dopant mass m, and Planck's constant h as follows:

$$\lambda_B = \frac{h^2}{m\varepsilon_d {r_{min}}^2} \quad (14)$$

Typical values are $\lambda_B > 1$ for light atoms (H−He, Li−He, and Na−He) with a significant zero-point energy and $\lambda_B < 0.15$ for heavy atoms and molecules (Ar−He and SF_6−He) where quantum mechanical effects only play a minor role.

dx.doi.org/10.1021/jp5034036 | J. Phys. Chem. A 2014, 118, 6622−6631

3. RESULTS AND DISCUSSION

We focus on a theoretical description of the interaction between a single Cr atom and He_{2000}. Besides the a^7S ground state of the atom, five electronic excitations of the Cr atom (z^7P, y^7P, a^5S, z^5P, and y^5P) are modeled and compared to recent experimental results of our group.[11−13] This section is divided into 6 subsections. We start with the discussion of the diatomic Cr−He PES[29] as basic requirements for the calculations. Second, we address the localization of the Cr on He_N in different electronic states and compare our DFT results to qualitative predictions based on the Ancilotto parameter. Third, the line shifts on optical excitation are calculated and their droplet size dependency is shown. Fourth, line broadening is discussed. Fifth, the size of the first solvation shell around ground state Cr (a^7S) is deduced. In the last subsection we compare our results to experimental data where possible.

3.1. Diatomic Cr−He Potential Energy Surfaces. The Cr−He PES for the $X^7\Sigma^+$ ground state (atomic a^7S state) and the $1^5\Sigma^+$ lowest quintet state (atomic a^5S) are taken from ref 29. In both cases, a Complete Active Space SCF (CASSCF) calculation was followed by a Davidson-corrected multireference calculation of second order (MRCI-Q). For the ground state, a powerful single-reference method (coupled cluster with singles, doubles, and perturbative triples (CCSD(T)))[47] could be applied as well for direct comparison. The resulting three PESs are plotted in Figure 2. All curves have been corrected for relativistic effects and extrapolated to the basis set limit.

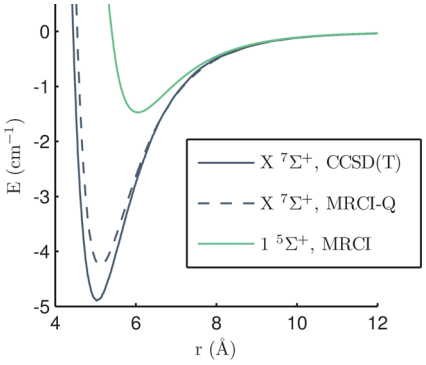

Figure 2. CCSD(T) and MRCI results for the PESs of Cr−He in the $X^7\Sigma^+$ ground state and the $1^5\Sigma^+$ lowest quintet state.

Although several electronically excited Cr−He PESs were available from ref 29, we decided to recalculate all of them together with the missing higher excitations in the quintet manifold. The inclusion of more excited states was only feasible at the cost of using a smaller basis set, in our case aug-cc-pVTZ-DK,[31,32] which necessitated the recalculation of all states for a more balanced description of both spin manifolds.

Figure 3 shows the PESs obtained for diatomic states with z^7P atomic limit ($2^7\Sigma^+$, $1^7\Pi$) and with z^5P atomic limit ($5^5\Sigma^+$,$5^5\Pi$). Note the big difference between Σ and Π PESs: $1^7\Pi$ and $5^5\Pi$ show a remarkably deep potential minimum, while $2^7\Sigma^+$ and the $5^5\Sigma^+$ do not. A similar behavior has been found for other species like copper, silver, and gold.[48−50] In contrast, states with y^7P atomic limit ($4^7\Sigma^+$, $4^7\Pi$) and with y^5P atomic limit ($6^5\Sigma^+$, $6^5\Pi$) show the typical shallow minimum as can be seen from Figure 4.

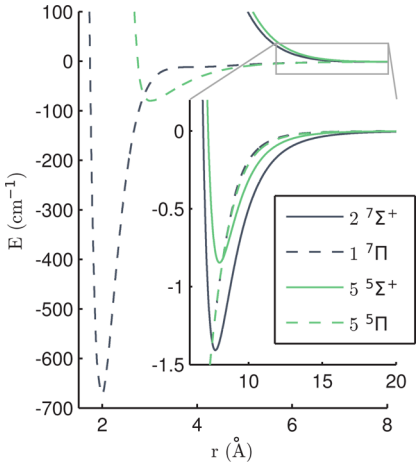

Figure 3. Comparison of Σ and Π states corresponding to z^7P and z^5P. Note the pronounced minima for $1^7\Pi$ and $5^5\Pi$.

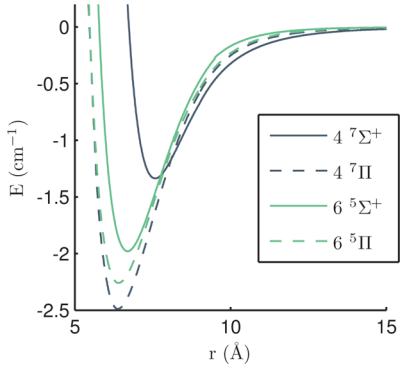

Figure 4. PESs for the excited Cr−He states $4^7\Sigma^+/4^7\Pi$ (y^7P) and $6^5\Sigma^+/6^5\Pi$ (y^5P).

The excited Cr−He states, $2^7\Sigma^+/1^7\Pi$ (z^7P), $4^7\Sigma^+/4^7\Pi$ (y^7P), $5^5\Sigma^+/5^5\Pi$ (z^5P), and $6^5\Sigma^+/6^5\Pi$ (y^5P), are mixed in pairs by the DIM approach to on-droplet Σ′ and Π′ states. Since the quintet and septet states show similar behavior, only the on-droplet septet states are shown in Figure 5. Because of the enormous difference in well depth between the shallow $2^7\Sigma^+$ and the deep $1^7\Pi$ PESs (z^7P), a cutoff at −3.5 cm^{-1} was chosen for the sake of illustration. The actual three-dimensional PES can be obtained by rotating the two-dimensional figures around the

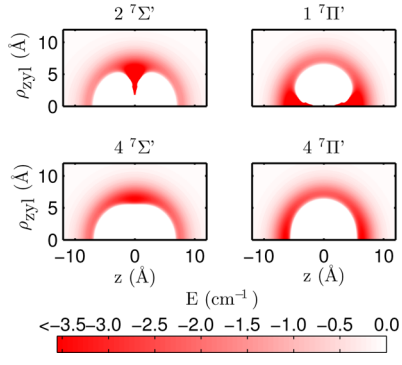

Figure 5. Contour plots of Σ′ and Π′ and the on-droplet PESs obtained from the DIM method for the $2^7\Sigma^+/1^7\Pi$ states (upper row) and $4^7\Sigma^+/4^7\Pi$ states (lower row), as a function of z and ρ_{zyl} for arbitrary φ. Energies are cut off at −3.5 cm^{-1} for clarity.

dx.doi.org/10.1021/jp5034036 | J. Phys. Chem. A 2014, 118, 6622−6631

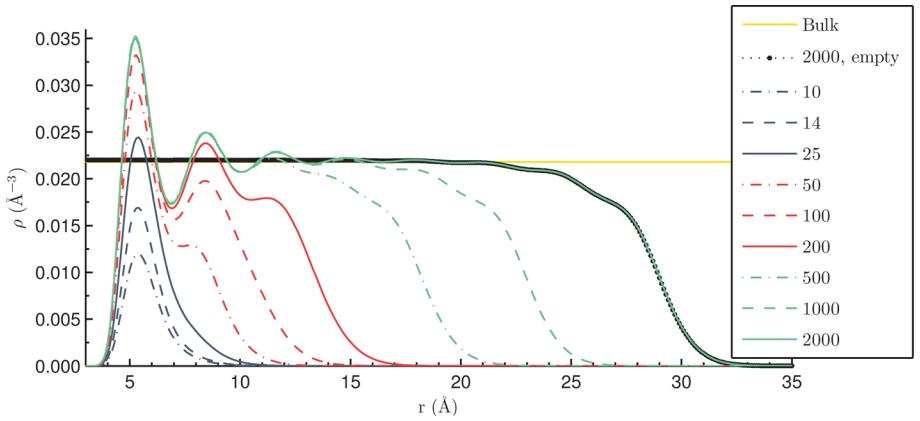

Figure 6. Density distributions for different He_N sizes doped with Cr in $X^7\Sigma'$ (a^7S) show a shell structure. Especially, a first and a second solvation shell at approximately 5.5 and 8.5 Å, respectively, are visible. Bulk density values are reached already for N = 500.

z axis. The Σ' PESs have a pronounced toroidal well around the Cr atom, in combination with the spherical shell of a local PES minimum. The Π' PES shows a similar spherical shell of local minimum but has pronounced global maxima on either side of the dopant along the z axis. Considering the on-droplet states corresponding to the z^7P and z^5P states it seems possible that exciplexes can be formed by trapping He atoms in the deep potential minima.[50]

3.2. Localization of Cr on He_N. We start with the calculation of Ancilotto parameters (λ_A) for the diatomic Cr−He PES as discussed in section 3.1. They are shown in Table 1, together with the essential parameters of the PES (minimum ϵ_d and equilibrium distance r_{min}) and the solvation de Boer factor (λ_B). The calculated λ_A indicate a submerged position of Cr−He in the $X^7\Sigma^+$ (a^7S) ground state and the strongly bound Π states, $1^7\Pi$ (z^7P) and $5^5\Pi$ (z^5P). All other states show a surface residing position of the dopant. However, considering elements with similar diatomic potential energy surfaces, such as Mg,[40,51−54] the behavior of Cr on He_N cannot be determined reliably. Therefore, we switch to the DFT approach for further investigation. In Figure 6, the calculated He_N density distributions of ground state Cr centered in He_N for N ranging from 10 to 2000 are compared to the undoped He_{2000} and bulk liquid He, using the ground state interaction potential for this study. Density peaks close to the dopant indicate a shell structure, which we discuss in section 3.5.

The density of the undoped He_{2000} is almost identical with the bulk liquid He density up to a radius of 21.5 Å, but then drops with small oscillations over a length of 10.5 Å to zero. In the case of the doped He_{2000}, the Cr atom pushes the He away and forms a bubble (zero He density) with a radius of 3.6 Å. A steep increase in He density can be seen near the rim of this bubble, with a maximum of 160% of bulk He density at 5.2 Å. This density peak aligns well with the minimum of the Cr−He PES (5.0 Å). It is followed by decaying density oscillations, but after the fourth density maximum at 16.4 Å the oscillations become barely visible at the given scale. From there, the doped and undoped He_{2000} density distributions are essentially the same.

For quantitative analysis, the Cr−He_{2000} PES is investigated for the states $X^7\Sigma'$ (a^7S) and $4^7\Sigma'/4^7\Pi'$ (y^7P), see Figure 7, and $1^5\Sigma'$ (a^5S) and $6^5\Sigma'/6^5\Pi'$ (y^5P), see Figure 8. The Cr−He_{2000} PES was determined by minimizing the energy functional in eq 1, including only the first and second term and subtracting the energy of the empty He_{2000}. On the basis of these Cr−He_{2000} PESs, the localization of the dopant can be seen by minimization of the solvation energy. Starting with the Cr−He_{2000} ground state $X^7\Sigma'$ (a^7S), we compare the effect of different Cr−He PES, CCSD(T), and MRCI-Q, on the Cr−He_{2000} system. These PESs have their minimum in solvation energy of −52.9 and −41.0 cm^{-1} in the center of the droplet for the CCSD(T) and MRCI-Q Cr−He PESs, respectively. Since the Cr−He ground state is treated more accurately by CCSD(T) than MRCI-Q,[29] the CCSD(T) results should be favored. Both Cr−He_{2000} PES show a typical behavior of

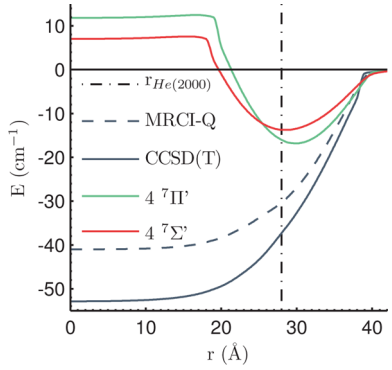

Figure 7. Cr−He_{2000} PESs for the $X^7\Sigma'$ (a^7S) and excited $4^7\Sigma'/4^7\Pi'$ (y^7P) states. $X^7\Sigma'$: comparison of CCSD(T) and MRCI-Q PESs from Figure 2; Cr resides inside He_N. $4^7\Sigma'/4^7\Pi'$: a surface residing position of the dopant is favored. A value of zero is approached at large radii, the energy of the relaxed He_{2000} without interaction with Cr.

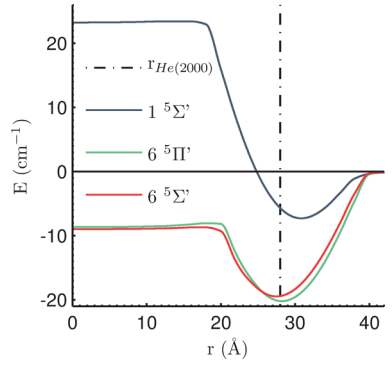

Figure 8. Cr−He_N PESs of the $1^5\Sigma'$ (a^5S) and $6^5\Sigma'/6^5\Pi'$ (y^5P) states; all states show a localization of the dopant close to the surface. Zero point of energy marks the empty He_{2000}.

dx.doi.org/10.1021/jp5034036 | J. Phys. Chem. A 2014, 118, 6622−6631

submerging dopants. The PES is nearly flat inside the droplet, with the inner 45% of the droplet radius showing an energy increase of at most 1.0%. Reaching the droplet radius of 28 Å, the solvation energy increases by 30%. The solvation energy approaches zero at ∼12 Å outside the droplet radius. This slow increase in solvation energy is associated with the abating He density around the droplet radius.

Two on-droplet excited states, $4^7\Sigma'/4^7\Pi'$ (y^7P), are depicted in the same figure (Figure 7). In contrast to the ground state $X^7\Sigma'$ (a^7S), these excited states favor a surface residing position ($4^7\Sigma'$, −13.7 cm^{-1} at 28 Å; $4^7\Pi'$, −16.8 cm^{-1} at 30 Å). This is indicated by a global minimum of the Cr−He_{2000} PES close to the surface and positive solvation energies upon full submersion of the dopant. However, a stable surface residing position can only be obtained if the excess energy, due to an on-droplet position of the Cr atom on excitation, can be dissipated into He_N without destroying it.

In the quintet manifold (see Figure 8), the Cr−He_{2000} PES of the lowest lying state $1^5\Sigma'$ (a^5S) indicates a surface residing position (−7.2 cm^{-1} at 31 Å). The $6^5\Sigma'/6^5\Pi'$ (y^5P) PES shows the interesting feature of a double minimum and are practically identical within less than 1 cm^{-1}. The local minimum (∼−9 cm^{-1}) is found in the droplet center. A tiny barrier of less than 1 cm^{-1} separates it from the global minimum (∼−20 cm^{-1}), which occurs close to the droplet surface at about 28 Å.

3.3. Line Shifts in Optical Excitation Spectra. The frozen droplet approximation was applied to calculate shifts in the transition energies for the $z^7P \leftarrow a^7S$, $y^7P \leftarrow a^7S$, $z^5P \leftarrow a^5S$, and $y^5P \leftarrow a^5S$ absorption bands. Starting from the on-droplet ground state $X^7\Sigma'$ (a^7S), the Cr atom is found within the He_N. An excitation into the $2^7\Sigma'/1^7\Pi'$ (z^7P) states requires an excess energy of 340 cm^{-1} for a vertical excitation within the DIM picture. The excitation into the $4^7\Sigma'/4^7\Pi'$ (y^7P) shows an even more distinct blue shift of 390 cm^{-1}. Figure 9 shows the

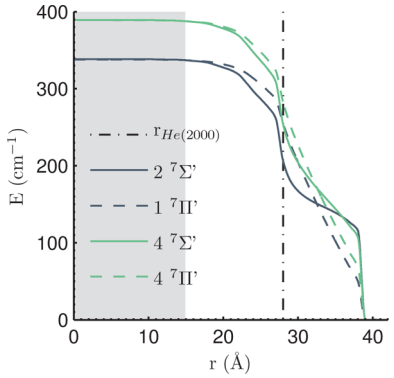

Figure 9. Transition energy shifts in the septet manifold: $2^7\Sigma'/1^7\Pi' \leftarrow X^7\Sigma'$ ($z^7P \leftarrow a^7S$) and $4^7\Sigma'/4^7\Pi' \leftarrow X^7\Sigma'$ ($y^7P \leftarrow a^7S$); the vertical transition region is marked in gray. A blueshift of 340 and 390 cm^{-1} is expected. The zero-line is the energy of the free-atom transition.

dependency of this energy shift on the position of the Cr on He_{2000} for the four septet states. For smallest deviations from the center position, the spherical symmetry of the bubble is almost conserved, leading to identical shifts for excited Σ′ and Π′ potentials. With increasing distance, their difference in shape becomes more and more important and leads to a split in energy. Small steps in the transition energy shift occur due to the interference of He_N density fluctuations with the interaction potential.

A different scenario is found in the quintet system, where the initial state is the surface residing $1^5\Sigma'$ (a^5S) state. The shifts of the transition into the four quintet states $5^7\Sigma'/5^7\Pi'$ (z^5P) and $6^7\Sigma'/6^7\Pi'$ (y^5P) are shown in Figure 10.

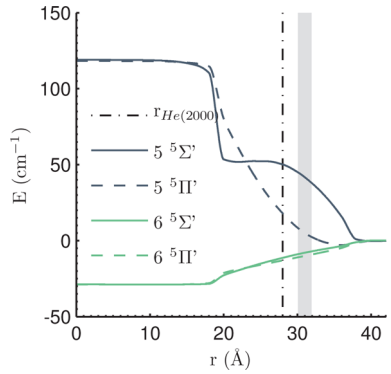

Figure 10. Transition energy shifts in the quintet manifold: the Cr atom is surface residing at around 33 Å (the vertical transition region is marked as a gray bar). A blueshift of 38 and 2 cm^{-1} is expected for the $5^5\Sigma'/5^5\Pi' \leftarrow 1^5\Sigma'$ ($z^5P \leftarrow a^5S$) transitions. A redshift of 7 and 9 cm^{-1} is found for the $6^5\Sigma'/6^5\Pi' \leftarrow 1^5\Sigma'$ ($y^5P \leftarrow a^5S$). Zero point of energy marks the free Cr atom.

A description in the pseudo-diatomic picture is appropriate because of the out-of-center location. At 31 Å, the equilibrium position of the $1^5\Sigma'$ (a^5S) state, the transition into the $5^5\Sigma'$ state, is blueshifted by 38 cm^{-1}. A minimal blueshift of 2 cm^{-1} is found for the $5^5\Pi' \leftarrow 1^5\Sigma'$ transition. The $6^5\Sigma'/6^5\Pi'$ (y^5P) states, however, show a slight redshift of 7 and 9 cm^{-1}, respectively. Their potential well is deeper and occurs at slightly larger equilibrium distance than $1^5\Sigma'$ (a^5S).

Since a He_N size distribution is found in experiments rather than a single He_N size, the droplet-size dependency of this blueshift was studied in the septet manifold, see Figure 11. The

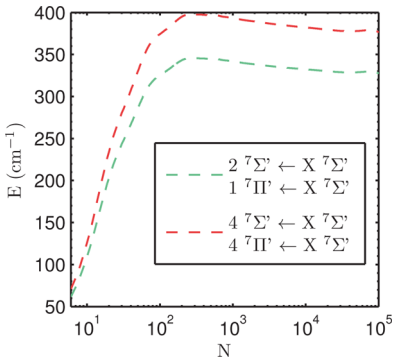

Figure 11. Droplet size dependence of the transition energy shift for the two transitions $2^7\Sigma'/1^7\Pi' \leftarrow X^7\Sigma'$ ($z^7P \leftarrow a^7S$) and $4^7\Sigma'/4^7\Pi' \leftarrow X^7\Sigma'$ ($y^7P \leftarrow a^7S$) in the frozen droplet approximation with the Cr atom in the droplet center. The blueshift on excitation remains fairly constant for $N > 200$.

Cr atom was placed in the center of He_N with 6 to 10^5 He atoms, and the vertical transition from the $X^7\Sigma'$ (a^7S) state into the $2^7\Sigma'/1^7\Pi'$ (z^7P) and $4^7\Sigma'/4^7\Pi'$ (y^7P) states was investigated. Because of the centered Cr atom, the on-droplet Σ′ and Π′ laser transitions are completely indistinguishable. The blueshift rises steeply for small He_N but remains fairly constant at 335(10) cm^{-1} (z^7P) and 385(10) cm^{-1} (y^7P) for

dx.doi.org/10.1021/jp5034036 | J. Phys. Chem. A 2014, 118, 6622−6631

He_N with $N > 200$. However, droplet sizes in experiments are usually considerably larger than 200 He atoms.[11−13]

The interaction of Cr with small He_N, including 6 (He_6) and 12 (He_{12}) He atoms, was also investigated based on CCSD(T) calculations with aug-cc-pVTZ-DK basis sets including DK correction. The interaction between the He atoms is included on a quantum mechanical level as well as the Cr−He interaction. This is a difference to the DFT approach where the Cr−He interaction is only considered by a diatomic potential. The calculation therefore includes many body interactions between Cr atom and several He atoms. The He atoms were fixed to the corners of a regular octahedron (He_6) and a regular icosahedron (He_{12}). The energy was calculated for various radii of the octahedron and the icosahedron resulting in the PESs shown in Figure 12. The minima of these

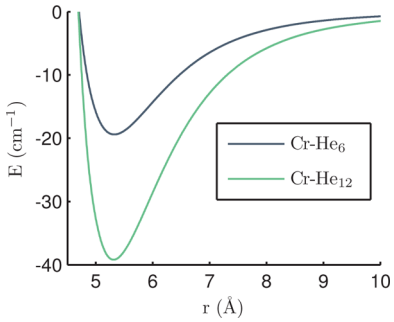

Figure 12. Cr−He_6 (octahedron) and Cr−He_{12} (icosahedron) PESs calculated with CCSD(T) based on aug-cc-pVTZ-DK basis sets; r is the distance between the centered Cr atom and the He atoms.

Cr−He_6 and Cr−He_{12} PESs are found at −19.4 and −39.2 cm^{-1}, respectively, and the equilibrium radii lie in the range between 5.3 to 5.5 Å for both PESs. In comparison, the DFT calculations show a solvation energy of −14.7 cm^{-1} for Cr−He_6 and −30.5 cm^{-1} for Cr−He_{12}. The equilibrium distances in Figure 11 (5.5 Å for both systems) are in good agreement with the position of the first density peak (see Figure 14a).

3.4. Line Broadening. Besides the blueshift, also line broadening is observed in experiments.[11−13] A line broadening due to the droplet-size dependency of the transition energy can usually be neglected. The experimental droplet-size distributions are peaked around 2000.[11] In this range, the size dependency of the blueshift is negligible, as can be seen in Figure 11. Thermal motion of the dopant within the He_N, also gives no significant contribution to line broadening. The wave function of Cr within He_{2000} extends to about ∼10 Å for the droplet temperature. There is only a small change in transition energy for such a displacement, see gray area in Figure 9. A large contribution to line broadening can be expected from deformations and oscillations of the bubble in He_N around the dopant. The breathing mode of the He_N bubble should dominate the line broadening[40] and was considered by the approach outlined in section 2.3. On the basis of these calculations, the hydrodynamic mass and the ground state energy of the breathing mode is found to be $M_0^* = ∼99$ u and $\omega_0 = ∼14.2$ cm^{-1}, respectively. In Figure 13, the spectra computed with eq 12 is compared to experimental values taken from ref 12. The breathing mode bubble oscillations lead to a line broadening of ∼200 cm^{-1} for the $4^7\Sigma'/4^7\Pi' \leftarrow X^7\Sigma'$ ($y^7P \leftarrow a^7S$) transition. Spin−orbit splitting and relative intensities are taken from the NIST database[55] and combined with our

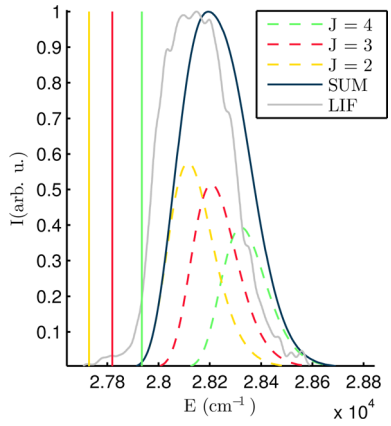

Figure 13. Comparing the experimental (LIF[12]) and theoretical spectra (SUM) for the $4^7\Sigma'/4^7\Pi' \leftarrow X^7\Sigma'$ ($y^7P \leftarrow a^7S$) transition; for the theoretical spectra, the spin−orbit splitting was included by taking the atomic values from NIST database into account.[55]

results for improved accuracy. This consideration leads to an even higher line broadening of about ∼350 cm^{-1} with a maximum at ∼28 200 cm^{-1}. Compared to the atomic line center at 27 847.78 cm^{-1}, a shift of ∼350 cm^{-1} is found. The overestimation of the line shift may be caused by neglecting the quadrupole deformation, see ref 40.

3.5. Solvation Shell. Density profiles of the He_N show a distinct shell-like structure around Cr dopants, see Figure 6. The first solvation shell is indicated by the global density maximum at 5.5 Å and a second solvation shell emerges at ∼8.3 Å. To deduce the number of the atoms in the first solvation shell, first the depicted density distributions of He_{10} to He_{14} around a Cr atom were calculated (Figure 14a). The size of the first solvation shell can be determined by adding He atoms one by one and watching how the normalized distribution $\rho(N)/N$

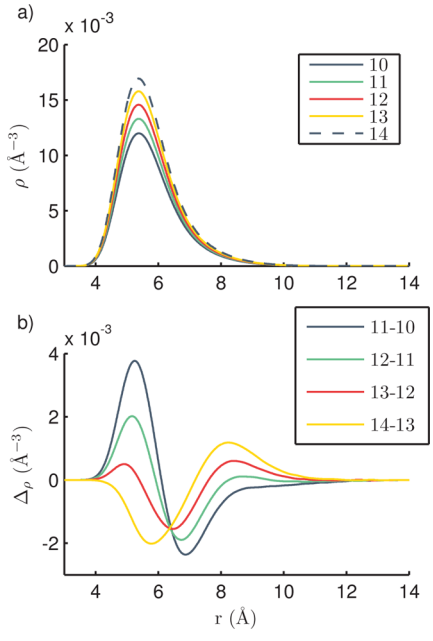

Figure 14. (a) Density profiles of He_{10} to He_{14}; (b) density profiles are normalized to their atom number, and the difference between the ascending droplet sizes are formed. The peak emerging at 8.3 Å indicates a first solvation shell of 12 He atoms.

dx.doi.org/10.1021/jp5034036 | J. Phys. Chem. A 2014, 118, 6622−6631

around the dopant evolves. Figure 13b shows a plot of the differences of normalized density distributions

$$\Delta_\rho = \frac{\rho(N)}{N} - \frac{\rho(N-1)}{N-1} \quad (15)$$

versus the coordinate r. Up to $N = 12$, Δ_ρ is negative at ∼8.3 Å, but beyond $N = 13$, the normalized density starts to rise, which indicates the beginning of a second shell formation at this position. The population of the second solvation shell, therefore, starts after 12 He atoms are accumulated in the first shell.

3.6. Comparison to Experiment. Experimentally, a band shift of about 300 cm^{-1} to the blue is found[11−13] for the transitions $z^7P \leftarrow a^7S$ and $y^7P \leftarrow a^7S$. This is in good agreement with our theoretical values of 340 cm^{-1} ($z^7P \leftarrow a^7S$) and 390 cm^{-1} ($y^7P \leftarrow a^7S$). The line broadening of the $y^7P \leftarrow a^7S$ transition was treated separately by including He bubble oscillations leading to a shift of ∼350 cm^{-1} and a broadening of ∼350 cm^{-1}. After excitation into the states z^7P and y^7P, sharp lines are observed in successive photo ionization[11] and fluorescence spectra[12] and interpreted as resulting from ejected free Cr atoms. We can confirm this interpretation for the y^7P, where the Cr atom is pushed to the He_N surface after excitation and may even leave the He_N. The probability of Cr captured in a surface residing position could not be determined and will depend on the distribution of excess energy after excitation into a number of different channels. For example, laser excitation from the Cr ground state into $4^7\Sigma'/4^7\Pi'$ (y^7P) in the "frozen He" approximation leaves the excited Cr atom with an excess energy of 390 − 8 = 382 cm^{-1}, compared to the equilibrium situation in which the helium environment would have readjusted to the excited Cr orbital. Even in the equilibrium situation, the solvation energy would be positive and not favor an inside location. The excess energy has to be distributed into helium modes and kinetic energy of the Cr atom. In this case, it is unlikely that the atom arrives at the surface with an energy low enough to be captured in the potential minimum of approximately 15 cm^{-1} well depth. A different case may be observable if Cr in its metastable a^5S state could be attached to a droplet and excited from the corresponding $1^5\Sigma'$ state into $6^5\Sigma'/6^5\Pi'$, which is also bound to the surface.

4. CONCLUSIONS

The interaction between Cr and He_N was investigated by density functional calculations for the He density[24] based on recently calculated diatomic Cr−He PESs.[29] The localization of the Cr atom on He_{2000} and expected shifts of transition energies due to Cr−He_N interaction were studied for the following atomic Cr states: a^7S, z^7P, y^7P, a^5S, z^5P, and y^5P. A droplet size dependency was investigated for the septet system. The solvation energy was calculated as a function of the Cr−He_N distance. On the basis of the ground state Cr−He_{2000} PES $X^7\Sigma'$ (a^7S), we showed that Cr resides inside He_N with a solvation energy of −53 cm^{-1}. Because of the nonspherically symmetric Cr−He_N interaction of the excited states, the diatomics in molecules approach (DIM) was applied when required. The Cr−He_{2000} states $4^7\Sigma'$ and $4^7\Pi'$ (y^7P) are surface residing with a binding energy of −14 and −17 cm^{-1} at an equilibrium distance of 28 and 30 Å, respectively. Transitions from the ground state $X^7\Sigma'$ (a^7S) into the excited septet states, $2^7\Sigma'/1^7\Pi'$ (z^7P) and $4^7\Sigma'/4^7\Pi'$ (y^7P), show a blueshift of 340 and 390 cm^{-1}, respectively. A droplet size dependency of the blueshift was investigated but found only to be significant for droplet sizes up to 200 He atoms. Line broadening based on the breathing mode bubble oscillation was found to be ∼350 cm^{-1} for the $4^7\Sigma'/4^7\Pi' \leftarrow X^7\Sigma'$ ($y^7P \leftarrow a^7S$) transition.

The shifts of transition energies were also investigated for quintet states. The lowest quintet state $1^5\Sigma'$ (a^5S) is surface residing at 31 Å and weakly bound with an energy of −7.2 cm^{-1}. The excited states $6^5\Sigma'$ and $6^5\Pi'$ (y^5P) are also found at the surface both at 28 Å with binding energies of −19 and −20 cm^{-1}, respectively. Besides the surface location, also a local minimum of −9 cm^{-1} inside He_N was found for both states. The transition energy shifts starting from the lowest lying quintet state $1^5\Sigma'$ are small compared to the septet system due to the surface residing position of the initial state.

Density profiles for the droplet-centered $X^7\Sigma'$ (a^7S) show a shell structure and a growth of the second solvation shell after 12 He atoms.

AUTHOR INFORMATION

Corresponding Authors

*(M.R.) E-mail: martin.ratschek@tugraz.at.

*(W.E.E.) E-mail: wolfgang.ernst@tugraz.at.

Notes

The authors declare no competing financial interest.

ACKNOWLEDGMENTS

The authors thank Andreas Kautsch for providing and discussing experimental data. This research was supported by the Austrian Science Fund (FWF) under Grant No. 22962-N20 as well as the European Commission and the Styrian Government within the ERDF program.

REFERENCES

(1) Knickelbein, M. B. Photoionization studies of chromium clusters: Ionization energies of Cr_4 to Cr_{25}. *Phys. Rev. A* **2003**, *67*, 013202.

(2) Payne, F. W.; Jiang, W.; Bloomfield, L. A. Magnetism and magnetic isomers in free chromium clusters. *Phys. Rev. Lett.* **2006**, *97*, 193401.

(3) Hauser, A. W.; Callegari, C.; Ernst, W. E. In *Advances in the Theory of Atomic and Molecular Systems: Dynamics, Spectroscopy, Clusters, and Nanostructures*; Piecuch, P., Maruani, J., Delgado-Barrio, G., Wilson, S., Eds.; Progress in Theoretical Chemistry and Physics; Springer Science+Business Media B.V.: New York, 2009; Chapter Level-Structure and Magnetic Properties from One-Electron Atoms to Clusters with Delocalized Electronic Orbitals: Shell Model for Alkali Trimers, Vol. *20*, pp 201−215.

(4) Callegari, C.; Ernst, W. E. In *Handbook of High Resolution Spectroscopy*, 1st ed.; Merkt, F., Quack, M., Eds.; John Wiley & Sons: New York, 2011; Chapter Helium Droplets as Nanocryostats for Molecular Spectroscopy: From the Vacuum Ultraviolet to the Microwave Regime, Vol. 3, pp 1551−1594.

(5) Hauser, A. W.; Auböck, G.; Callegari, C.; Ernst, W. E. Relativistic Jahn−Teller effects in the quartet states of K_3 and Rb_3: A vibronic analysis of the $2^4E' \leftarrow 1^4A^{2'}$ electronic transitions based on ab initio calculations. *J. Chem. Phys.* **2010**, *132*, 164310.

(6) Nagl, J.; Auböck, G.; Hauser, A. W.; Allard, O.; Callegari, C.; Ernst, W. E. High-spin alkali trimers on helium nanodroplets: Spectral separation and analysis. *J. Chem. Phys.* **2008**, *128*, 154320.

(7) Nagl, J.; Auböck, G.; Hauser, A. W.; Allard, O.; Callegari, C.; Ernst, W. E. Heteronuclear and Homonuclear high-spin alkali trimers on helium nanodroplets. *Phys. Rev. Lett.* **2008**, *100*, 063001.

(8) Przystawik, A.; Radcliffe, P.; Gode, S. G.; Meiwes-Broer, K. H.; Tiggesbaumker, J. Spectroscopy of silver dimers in triplet states. *J. Phys. B: At. Mol. Opt. Phys.* **2006**, *39*, S1183−S1189.

(9) Toennies, J. P.; Vilesov, A. F. Superfluid helium droplets: a uniquely cold nanomatrix for molecules and molecular complexes. *Angew. Chem., Int. Ed.* **2004**, *43*, 2622−2648.
(10) Ratschek, M.; Koch, M.; Ernst, W. E. Doping helium nanodroplets with high temperature metals: Formation of chromium clusters. *J. Chem. Phys.* **2012**, *136*, 104201.
(11) Kautsch, A.; Hasewend, M.; Koch, M.; Ernst, W. E. Fano resonances in chromium photoionization spectra after photoinduced ejection from a superfluid helium nanodroplet. *Phys. Rev. A* **2012**, *86*, 033428.
(12) Kautsch, A.; Koch, M.; Ernst, W. E. Electronic relaxation after resonant laser excitation of Cr in superfluid helium nanodroplets. *J. Phys. Chem. A* **2013**, *117*, 9621−9625.
(13) Koch, M.; Kautsch, A.; Lackner, F.; Ernst, W. E. One- and Two-Color Resonant Photoionization Spectroscopy of Chromium Doped Helium Nanodroplets. *J. Phys. Chem. A* **2014**, DOI: 10.1021/jp501285r.
(14) Ceperley, D. M.; Mitas, L. In *New Methods in Computational Quantum Mechanics*; Prigogine, I., Rice, S. A., Eds.; Advances in Chemical Physics; John Wiley & Sons, Inc.: New York, 1996; Chapter Quantum Monte Carlo Methods in Chemistry, Vol. *XCIII*, pp 1−38.
(15) Rodriguez-Cantano, R.; Lopez-Duran, D.; Gonzalez-Lezana, T.; Delgado-Barrio, G.; Villarreal, P.; Yurtsever, E.; Gianturco, F. A. Spin-Polarized Rb_2 Interacting with Bosonic He Atoms: Potential Energy Surface and Quantum Structures of Small Clusters. *J. Phys. Chem. A* **2012**, *116*, 2394−2404.
(16) Rodriguez-Cantano, R.; de Tudela, R. P.; Lopez-Duran, D.; Gonzalez-Lezana, T.; Gianturco, F. A.; Delgado-Barrio, G.; Villarreal, P. Quantum rotation of Rb_2 ($^3\sum_u^+$) attached to He_N droplets: a path-integral Monte Carlo study. *Eur. Phys. J. D* **2013**, *67*, 119.
(17) Hauser, A. W.; Gruber, T.; Filatov, M.; Ernst, W. E. Shifts in the ESR Spectra of Alkali-Metal Atoms (Li, Na, K, Rb) on Helium Nanodroplets. *ChemPhysChem* **2013**, *14*, 716−722.
(18) Poms, J.; Hauser, A. W.; Ernst, W. E. Helium nanodroplets doped with xenon and rubidium atoms: A case study of Van der Waals interactions between heliophilic and heliophobic dopants. *Phys. Chem. Chem. Phys.* **2012**, *14*, 15158−15165.
(19) Barranco, M.; Guardiola, R.; Hernandez, S.; Mayol, R.; Navarro, J.; Pi, M. Helium nanodroplets: An overview. *J. Low Temp. Phys.* **2006**, *142*, 1−81.
(20) Dupontroc, J.; Himbert, M.; Pavloff, N.; Treiner, J. Inhomogeneous liquid ^{4}He: A density functional-approach with a finite-range interaction. *J. Low Temp. Phys.* **1990**, *81*, 31−44.
(21) Weisgerber, S.; Reinhard, P. G. The shell structure of ^{3}He droplets. *Z. Phys. D: At., Mol. Clusters* **1992**, *23*, 275−282.
(22) Barranco, M.; Jezek, D. M.; Hernandez, E. S.; Navarro, J.; Serra, L. L. A density functional for liquid ^{3}He. *Z. Phys. D: At., Mol. Clusters* **1993**, *28*, 257−268.
(23) Garcia-Recio, C.; Navarro, J.; Nguyen, V. G.; Salcedo, L. L. Response functions for infinite fermion systems with velocity dependent interactions. *Ann. Phys.* **1992**, *214*, 293−340.
(24) Dalfovo, F.; Lastri, A.; Pricaupenko, L.; Stringari, S.; Treiner, J. Structural and dynamical properties of superfluid helium: A density-functional approach. *Phys. Rev. B* **1995**, *52*, 1193−1209.
(25) Callegari, C.; Lehmann, K. K.; Schmied, R.; Scoles, G. Helium nanodroplet isolation rovibrational spectroscopy: Methods and recent results. *J. Chem. Phys.* **2001**, *115*, 10090−10110.
(26) Lehmann, K. K.; Callegari, C. Quantum hydrodynamic model for the enhanced moments of inertia of molecules in helium nanodroplets: Application to SF_6. *J. Chem. Phys.* **2002**, *117*, 1595−1603.
(27) Ancilotto, F.; Barranco, M.; Caupin, F.; Mayol, R.; Pi, M. Freezing of ^{4}He and its liquid-solid interface from density functional theory. *Phys. Rev. B* **2005**, *72*, 214522.
(28) Mateo, D.; Hernando, A.; Barranco, M.; Loginov, E.; Drabbels, M.; Pi, M. Translational dynamics of photoexcited atoms in ^{4}He nanodroplets: the case of silver. *Phys. Chem. Chem. Phys.* **2013**, *15*, 18388−18400.
(29) Pototschnig, J. V.; Ratschek, M.; Hauser, A. W.; Ernst, W. E. An ab intio study of the CrHe diatomic molecule: The effect of van der Waals distortion on a highly magnetic multi-electron system. *Phys. Chem. Chem. Phys.* **2014**, *16*, 9469−9478.
(30) Werner, H.-J.; Knowles, P. J.; Knizia, G.; Manby, F. R.; Schütz, M.; Celani, P.; Korona, T.; Lindh, R.; Mitrushenkov, A.; Rauhut, G.; et al. *MOLPRO*, version 2012.1, a package of ab initio programs, 2012; see http://www.molpro.net/.
(31) Balabanov, N. B.; Peterson, K. A. Systematically convergent basis sets for transition metals. I. All-electron correlation consistent basis sets for the 3d elements Sc-Zn. *J. Chem. Phys.* **2005**, *123*, 064107.
(32) Woon, D. E.; Dunning, T. H. Gaussian-basis sets for use in correlated molecular calculations 0.4. Calculation of static electrical response properties. *J. Chem. Phys.* **1994**, *100*, 2975−2988.
(33) Knowles, P. J.; Werner, H.-J. Internally contracted multi-configuration reference configuration interaction calculations for excited states. *Theor. Chem. Acc.* **1992**, *84*, 95−103.
(34) Knowles, P. J.; Werner, H.-J. An efficient second-order MC SCF method for long configuration expansions. *Chem. Phys. Lett.* **1985**, *115*, 259−267.
(35) Pifrader, A.; Allard, O.; Auböck, G.; Callegari, C.; Ernst, W. E.; Huber, R.; Ancilotto, F. One- and two-photon spectroscopy of highly excited states of alkali-metal atoms on helium nanodroplets. *J. Chem. Phys.* **2010**, *133*, 164502.
(36) Ellison, F. O. Scaled diatomics-in-molecules (SDIM) theory. I. General theory and preliminary applications to H_3 and H_4. *J. Chem. Phys.* **1983**, *78*, 5024−5030.
(37) Ellison, F. O. A method of diatomics in molecules. I. General theory and application to H_2O. *J. Am. Chem. Soc.* **1963**, *85*, 3540−3544.
(38) Leino, M.; Viel, A.; Zillich, R. E. Electronically excited rubidium atom in helium clusters and films. II. Second excited state and absorption spectrum. *J. Chem. Phys.* **2011**, *134*, 024316.
(39) Hernando, A.; Barranco, M.; Mayol, R.; Pi, M.; Krosnicki, M. Absorption spectrum of Ca atoms attached to ^{4}He nanodroplets. *Phys. Rev. B* **2008**, *77*, 024513.
(40) Hernando, A.; Barranco, M.; Mayol, R.; Pi, M.; Ancilotto, F. Density functional theory of the structure of magnesium-doped helium nanodroplets. *Phys. Rev. B* **2008**, *78*, 184515.
(41) Bunermann, O.; Droppelmann, G.; Hernando, A.; Mayol, R.; Stienkemeier, F. Unraveling the absorption spectra of alkali metal atoms attached to helium nanodroplets. *J. Phys. Chem. A* **2007**, *111*, 12684−12694.
(42) Mella, M.; Colombo, M. C.; Morosi, G. Ground state and excitation dynamics in Ag doped helium clusters. *J. Chem. Phys.* **2002**, *117*, 9695−9702.
(43) Kinoshita, T.; Fukuda, K.; Yabuzaki, T. Doubly shaped D_2 excitation spectra of Cs and Rb atoms in superfluid helium due to a quadrupole bubble surface oscillation. *Phys. Rev. B* **1996**, *54*, 6600−6607.
(44) Ouboter, R. D. B.; Yang, C. N. The thermodynamic properties of liquid ^{3}He−^{4}He mixtures between 0 and 20 atm in the limit of absolute zero temperature. *Phys. B+C* **1987**, *144*, 127−144.
(45) Roche, P.; Deville, G.; Appleyard, N.; Williams, F. Measurement of the surface tension of superfluid ^{4}He at low temperature by capillary wave resonances. *J. Low Temp. Phys.* **1997**, *106*, 565−573.
(46) Ancilotto, F.; Lerner, P. B.; Cole, M. W. Physics of solvation. *J. Low Temp. Phys.* **1995**, *101*, 1123−1146.
(47) Watts, J. D.; Gauss, J.; Bartlett, R. J. Coupled-cluster methods with noniterative triple excitations for restricted open-shell Hartree−Fock and other general single determinant reference functions. Energies and analytical gradients. *J. Chem. Phys.* **1993**, *98*, 8718−8733.
(48) Cargnoni, F.; Kus, T.; Mella, M.; Bartlett, R. J. Ground state potential energy surfaces and bound states of M-He dimers (M═Cu,Ag,Au): A theoretical investigation. *J. Chem. Phys.* **2008**, *129*, 204307.
(49) Cargnoni, F.; Mella, M. Solubility of metal atoms in helium droplets: Exploring the effect of the well depth using the coinage metals Cu and Ag. *J. Phys. Chem. A* **2011**, *115*, 7141−7152.

(50) Cargnoni, F.; Ponti, A.; Mella, M. Coinage metal exciplexes with helium atoms: a theoretical study of $M^*(^2L)He_n$ (M = Cu, Ag, Au; L = P,D). *Phys. Chem. Chem. Phys.* **2013**, *15*, 18410−18423.
(51) Mella, M.; Calderoni, G.; Cargnoni, F. Predicting atomic dopant solvation in helium clusters: The $MgHe_n$ case. *J. Chem. Phys.* **2005**, *123*, 054328.
(52) Przystawik, A.; Gode, S.; Doppner, T.; Tiggesbaumker, J.; Meiwes-Broer, K. H. Light-induced collapse of metastable magnesium complexes formed in helium nanodroplets. *Phys. Rev. A* **2008**, *78*, 021202.
(53) Navarro, J.; Mateo, D.; Barranco, M.; Sarsa, A. Mg impurity in helium droplets. *J. Chem. Phys.* **2012**, *136*, 054301.
(54) Gode, S.; Irsig, R.; Tiggesbaumker, J.; Meiwes-Broer, K. H. Time-resolved studies on the collapse of magnesium atom foam in helium nanodroplets. *New J. Phys.* **2013**, *15*, 015026.
(55) Ralchenko, Y.; Kramida, A.; Reader, J.; NIST ASD Team. *NIST Atomic Spectra Database* (ver. 4.1.0) [Online]; National Institute of Standards and Technology: Gaithersburg, MD, 2011.